IJMMM International Journal of Minerals, Metallurgy and Materials 矿物冶金与材料学报（英文版）

Cobalt-based multicomponent nanoparticles supported on N-doped graphene as advanced cathodic catalyst for zinc–air batteries

Shanjing Liu, Xiaohan Wan, Yue Sun, Shiqi Li, Xingmei Guo, Ming Li, Rui Yin, Qinghong Kong, Jing Kong, and Junhao Zhang

Cite this article as:
Shanjing Liu, Xiaohan Wan, Yue Sun, Shiqi Li, Xingmei Guo, Ming Li, Rui Yin, Qinghong Kong, Jing Kong, and Junhao Zhang, Cobalt-based multicomponent nanoparticles supported on N-doped graphene as advanced cathodic catalyst for zinc–air batteries, *Int. J. Miner. Metall. Mater.*, 29(2022), No. 12, pp. 2212-2220. https://doi.org/10.1007/s12613-022-2498-0

International Journal of Minerals, Metallurgy and Materials
Volume 29, Number 12, December 2022, Page 2212
https://doi.org/10.1007/s12613-022-2498-0

Cobalt-based multicomponent nanoparticles supported on N-doped graphene as advanced cathodic catalyst for zinc–air batteries

Shanjing Liu[1),*], *Xiaohan Wan*[1),*], *Yue Sun*[1)], *Shiqi Li*[1)], *Xingmei Guo*[1),✉], *Ming Li*[1)], *Rui Yin*[1)], *Qinghong Kong*[2)], *Jing Kong*[3)], *and Junhao Zhang*[1),✉]

1) School of Environmental and Chemical Engineering, Jiangsu University of Science and Technology, Zhenjiang 212003, China
2) School of the Environment and Safety Engineering, Jiangsu University, Zhenjiang 212013, China
3) China Aerospace Components Engineering Center, China Academy of Space Technology, Beijing 100094, China
(Received: 4 March 2022; revised: 10 April 2022; accepted: 15 April 2022)

Abstract: To improve the efficiency of cathodic oxygen reduction reaction (ORR) in zinc–air batteries (ZABs), an adsorption–complexation–calcination method was proposed to generate cobalt-based multicomponent nanoparticles comprising Co, Co_3O_4 and CoN, as well as numerous N heteroatoms, on graphene nanosheets (Co/Co_3O_4/CoN/NG). The Co/Co_3O_4/CoN nanoparticles with the size of less than 50 nm are homogeneously dispersed on N-doped graphene (NG) substrate, which greatly improve the catalytic behaviors for ORR. The results show that the half-wave potential is as high as 0.80 V vs. RHE and the limiting current density is 4.60 $mA·cm^{-2}$, which are close to those of commercially available platinum/carbon (Pt/C) catalysts. Applying as cathodic catalyst for ZABs, the battery shows large specific capacity and open circuit voltage of 843.0 $mAh·g^{-1}$ and 1.41 V, respectively. The excellent performance is attributed to the efficient two-dimensional structure with high accessible surface area and the numerous multiple active sites provided by highly scattered Co/Co_3O_4/CoN particles and doped nitrogen on the carbon matrix.

Keywords: adsorption–complexation–calcination; cobalt-based multicomponent nanoparticles; N-doped graphene; oxygen reduction reaction; zinc–air batteries

1. Introduction

The fast development of modern society makes it necessary to explore efficient electrochemical devices for storing and converting energy [1–2]. Zinc–air batteries (ZABs) have drawn great attention because of their advantages of smooth discharging behavior, environmentally friendliness, high energy density, and inexpensiveness [3–4]. However, the cathodic oxygen reduction reaction (ORR) is slow in kinetics, and the performance of ZABs is largely determined by the electrocatalysts which promote their reaction efficiency [5]. At present, the most effective ORR catalyst is platinum-based precious metal materials, such as Pt alloys and Pt/C composites. In addition to being expensive and scarce in resources, these catalysts also have disadvantages of poor durability, low selectivity, and poor methanol tolerance. Therefore, it is particularly important to develop nonprecious ORR electrocatalysts with both high catalytic activity and stability. Among them, transition metals have a variety of compound configurations and exhibit adjustable electrocatalytic activity, which are frequently studied in electrocatalysis fields. In the past decades, the study of transition metal compounds (TMCs) as efficient electrochemical catalysts for ORR has become a research hotspot, including single TMC materials and multi-component TMCs materials [6–9].

Transition metal oxides have drawn great attention because of their high electrochemical stability, good ORR catalytic activity, and low cost. However, most transition metal oxides are insulators or semiconductors, which inhibit internal electron transfer and electron transfer between catalysts and supporting electrodes [10–12]. Hence, sole oxides as electrocatalysts often show high overpotential and low reaction efficiency. Compared with oxides, nitrides usually exhibit better conductivity because of the lower electronegativity of N than O atoms [13]. What's more, as nitrides tend to grow in the form of interstitial compounds, the distance between metal atoms increases and the d band shrinks, which leads to the increase of density of states near Fermi level and is conducive to electrocatalysis [14]. However, in many cases, the adsorbing ability of O_2 on nitrides is still weaker than that on oxides, which is not favorable for triggering ORR [15]. Therefore, combining nitrides and oxides into one integrated system is believed to be a worth trying approach to achieve high catalytic activity, together with relatively good conductivity [16–17]. In addition, the existence of metallic phases can also improve the electronic transport and promote

* These authors contribute equally to this work.
✉ Corresponding authors: Xingmei Guo E-mail: guoxm@just.edu.cn; Junhao Zhang E-mail: jhzhang6@just.edu.cn

the efficiency of electrocatalytic reactions [18–19]. However, it is a big challenge to construct systems comprising multiple components of oxide, nitride, and metallic phases in simple steps, whose synergistic effect may lead to optimized electrocatalytic performance for ORR.

In order to further promote the electron transport efficiency and increase the utilization ratio of active sites, compound based active species are usually supported on carbon matrix in practical research. Different carbonaceous materials with various microstructures have been unitized, such as carbon nanotubes [20], carbon nanofibers [21], mesoporous carbon [22], and graphene [23]. These microstructures can increase the electronic conductivity and facilitate mass transport during electrocatalysis. Thereinto, graphene has drawn great attention because of its large accessible surface area and outstanding stability [24–25] Moreover, introducing nonmetallic heteroatoms (e.g. N, S, P) into graphene lattice would regulate the electronic structure and generate new catalytic active sites, which further help to accelerate the ORR kinetics [26–28].

Herein, an adsorption–complexation–calcination method was devised to construct N-doped graphene (NG) loaded with $Co/Co_3O_4/CoN$ multicomponent nanoparticles. In the preparation process, Co^{2+} ions were adsorbed on graphene oxide (GO) followed by adding excessive amount of ammonia to form $[Co(NH_3)_6]^{2+}$ complex ions. After calcining in nitrogen, $[Co(NH_3)_6]^{2+}$ transformed into $Co/Co_3O_4/CoN$ multicomponent nanoparticles, and other adsorbed ammonia was doped into carbon lattice forming N-doped graphene (NG). The multiple catalytic active sites and efficient two-dimensional architecture lead to excellent electrocatalytic performance for ORR, making $Co/Co_3O_4/CoN/NG$ a promising cathode catalyst for ZABs.

2. Experimental

2.1. Materials synthesis

Firstly, 20 mL $CoCl_2$ (0.003 mol·L^{-1}) aqueous solution was poured into 20 mL GO dispersion solution (2 mg·mL^{-1}), followed by an ultrasound bath for 2 h. After centrifugal washing, the product was put into 30 mL deionized water again, followed by dropping 10 mL ammonia (25wt%–28wt%) into the solution and magnetically stirred for 1 h. After thorough reaction and adsorption, the sample was sequentially washed with water and ethylalcohol for three times, and freeze-dried for 24 h to obtain GO loaded with large amounts of $[Co(NH_3)_6]^{2+}$ complex ions and ammonia. Finally, the sample was calcined in N_2 to 700°C with a heating rate of 2°C·min^{-1} and held for 2 h to obtain the final $Co/Co_3O_4/CoN/NG$ composite. In addition, as a way of comparison, $Co/Co_3O_4/G$ and NG samples were also prepared using the same method, except without the addition of ammonia or $CoCl_2·6H_2O$ in the synthesizing process.

2.2. Materials characterization

Field emission scanning electron microscopy (FESEM) analysis and high-resolution transmission electron microscopy (HRTEM) analysis were performed with a Philips Zeiss Merlin microscope and a Philips JEM-2100F microscope, respectively, for observing the external appearance and internal structure of the products. X-ray diffractometer (XRD, XRD-6000X, Japan) and Raman spectrometer (Renishaw InVia 2000, Britain) were used to study the phase composition and crystal structure. In addition, X-ray photoelectron spectroscopy (XPS, AXIS UltraDLD, Japan) was used to investigate the elemental states of surface. The N_2 adsorption/desorption test was conducted on a Micro ASAP Metrics 2010 instrument at 77 K, for estimating the specific surface area and pore volume.

2.3. Electrochemical measurements

The electrocatalytic properties were tested in the electrolyte of N_2/O_2 saturated KOH solution (0.1 mol·L^{-1}), using the autolab electrochemical workstation (PGSTAT 30). Rotating disk electrode (RDE; diameter: 5 mm) carrying different catalyst materials, Ag/AgCl electrode, and graphite rod were applied as working, reference, and counter electrodes, respectively. The process of modifying the catalysts on RDE is as follows: First, 5.0 mg cathodic catalysts were dispersed in a solvent containing 725.0 μL deionized water, 250.0 μL ethylalcohol, and 25.0 μL Nafion (5.0wt%). Then, the mixture was ultrasonically treated for 0.5 h to prepare a uniform catalyst dispersion solution (5.0 mg·mL^{-1}). Finally, the working electrode was made through dripping 10.0 μL suspension on the RDE (0.25 mg·cm^{-2}) with solvent evaporated. As a contrast, Pt/C working electrode was prepared following the same process. Cyclic voltammetry (CV) was tested in electrolyte saturated with nitrogen or oxygen at 50.0 mV·s^{-1}. Linear sweep voltammetry (LSV) was carried out in O_2 saturated electrolyte at 10.0 mV s^{-1} with RDE rotated at 400–2025 r/min. Nyquist plots were investigated over the frequency range from 0.01 to 10^5 Hz, using the technique of electrochemical impedance spectroscopy (EIS). All potentials are converted to reversible hydrogen potentials (RHE) through superinducing a value of (0.197 + 0.059 × pH) V. Cycle lives were detected by chronoamperometry at the constant potential of 0.6 V vs. RHE. Methanol tolerance was estimated by dripping 5 mL methanol to 100 mL KOH electrolyte saturated with O_2 at about 400 s during chronoamperometry. According to the Koutecky–Levich (K–L) plot, the number (n) of electron transfer was appraised using the following equations [29–30]:

$$\frac{1}{J} = \frac{1}{J_L} + \frac{1}{J_K} \tag{1}$$

$$J_L = 0.620nFAC_o D_o^{2/3} \omega^{1/2} \nu^{-1/6} \tag{2}$$

$$J_K = nFkC_o \tag{3}$$

where J represents the tested current density in the ORR process; J_K refers to the kinetic current density and J_L stands for the limiting current density; A is the area of the electrode; ω is the rotational speed of RDE; n represents the number of electron transfers; F, C_o, D_o, and ν are all constants, and their values in the system are 96485 C·mol^{-1}, 1.2 × 10^{-3} mol·cm^{-3}, 1.9 × 10^{-5} cm^2·s^{-1}, and 0.01 cm^2·s^{-1}, respectively; k represents the rate constant for electron transfer with a value of 0.2 when r/min is used as dimension unit for ω.

2.4. Zinc–air battery construction and measurements

1.0 mg $Co/Co_3O_4/CoN$ nanoparticles and 0.25 mg acetylene black were added into the mixed solution composed of 10 μL Nafion and 0.25 mL ethanol. The mixture was then ultrasonically treated for 1 h to get a homogeneous dispersion, and the dispersion was dripped on 1 cm^2 area of hydrophobic carbon paper (1 $mg \cdot cm^{-2}$) and used as cathode after solvent evaporation. Zn plate was applied as anode; the aqueous solution of KOH (6 $mol \cdot L^{-1}$) + $Zn(CH_3COO)_2$ (0.2 $mol \cdot L^{-1}$) was used as electrolyte. After ZABs were assembled, the polarization curves were measured by LSV technique at 10 $mV \cdot s^{-1}$, and the whole testing process was carried out on Autolab electrochemical workstation. Wuhan LAND battery test system was employed to accomplish constant current discharge and rate capability tests.

3. Results and discussion

3.1. Characterization of composition and structure

Fig. 1(a) schematically illustrates the adsorption–complexation–calcination procedures to synthesize $Co/Co_3O_4/CoN/NG$. The SEM image of original GO is displayed in Fig. 1(b), which shows obvious nanosheet structure with smooth surface. For $Co/Co_3O_4/CoN/NG$, the morphology is almost the same as that of graphene (Fig. 1(c)). However, under TEM, nanoparticles can be distinguished on the nanosheets. As shown in Fig. 1(d), the sizes vary from 5 to 50 nm. Fig. 1(e)–(g) shows the lattice images of the dispersed nanoparticles. The lattice distances of 0.205, 0.244, and 0.482 nm agree well with the (111) plane of Co, (311) plane of Co_3O_4, and (111) plane of CoN, respectively, indicating that the nanoparticles loaded on graphene contain Co, Co_3O_4, and CoN components. Co, O, and N are mainly distributed in the region of the nanoparticles from the elemental mapping images in Fig. 1(h), while the matrix is mainly composed of C with a big amount of N and small amount of O. This further proves that the nanoparticles contain oxides and nitrides of cobalt, and the matrix is N-doped graphene sheet. Fig. S1 presents the X-ray energy dispersive spectrum (EDS) and relative contents of different elements, which agrees well with the above analysis.

XRD results for samples calcined at 700°C were studied to determine the phase and crystal structure. As shown in Fig. 2(a), all samples have bumps near 26° and 42°, which match well with (002) and (101) planes of the graphitized regions in GO [31–32]. For $Co/Co_3O_4/G$ and $Co/Co_3O_4/CoN/NG$, the diffraction peaks at 36.8° and 44.8° correspond to the (220) and (400) plane of Co_3O_4; the diffraction signals at 44.2° and 51.5° match with the (111) and (200) planes of Co. Moreover, two other diffraction peaks, corresponding to CoN (111) and CoN (220) faces, are observed at 42.1° and 61.3° for $Co/Co_3O_4/CoN/NG$. This suggests that the adsorbed Co^{2+} can be partly transformed into Co_3O_4, and partly transformed into Co without the addition of ammonia. When ammonia is

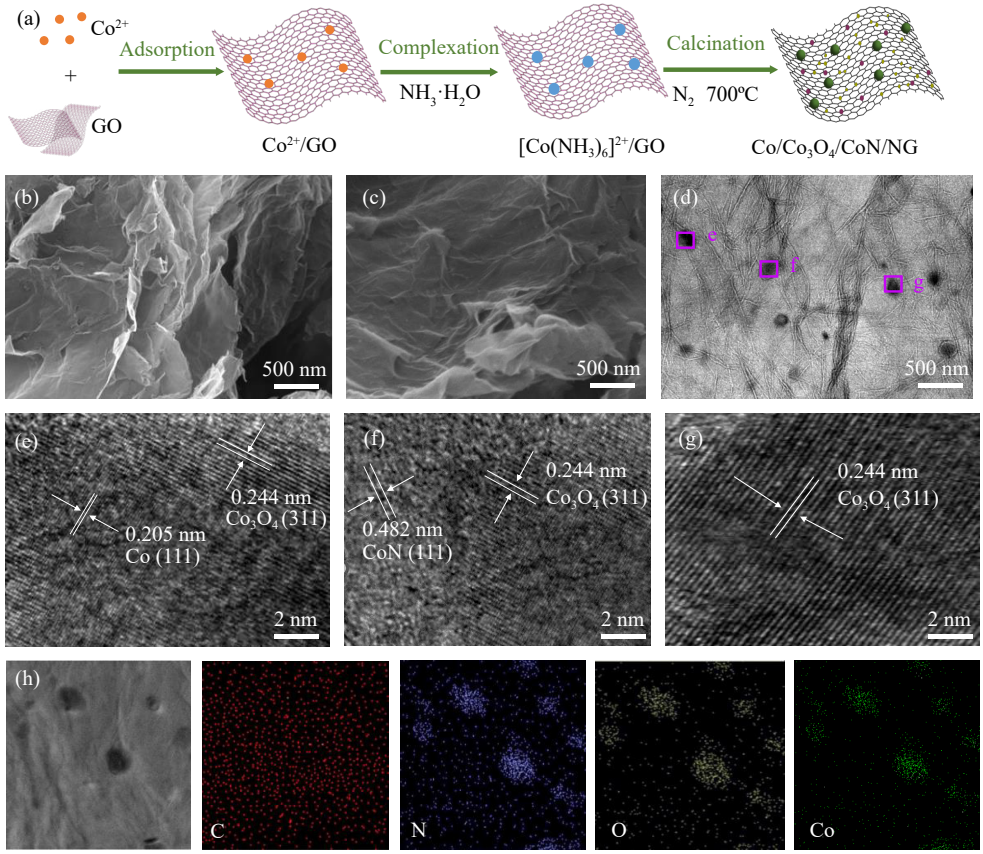

Fig. 1. (a) Schematic diagram of the synthesizing procedures of $Co/Co_3O_4/CoN/NG$; (b) FESEM image of GO; (c, d) SEM and TEM images of $Co/Co_3O_4/CoN/NG$; (e–g) HRTEM lattice images of the nanoparticles in $Co/Co_3O_4/CoN/NG$; (h) elemental mapping images of C, N, O, and Co in $Co/Co_3O_4/CoN/NG$.

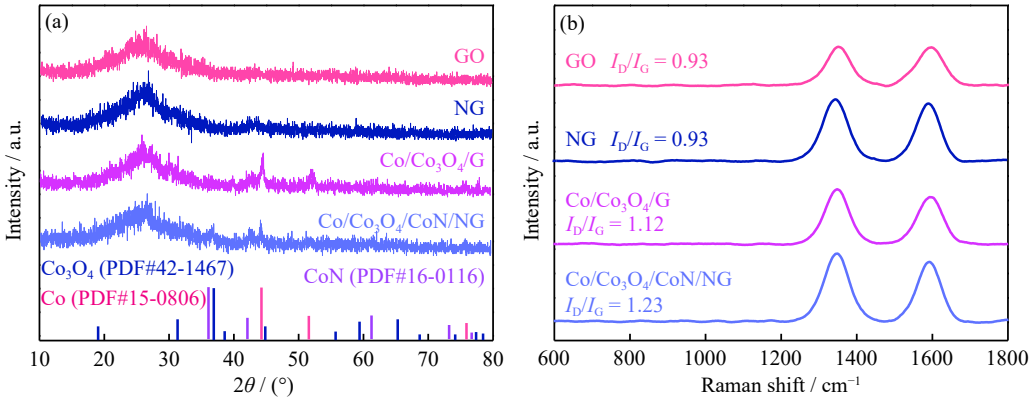

Fig. 2. (a) XRD and (b) Raman patterns of GO, NG, $Co/Co_3O_4/G$, and $Co/Co_3O_4/CoN/NG$.

added, Co^{2+} and NH_4^+ coordinate to form $[Co(NH_3)_6]^{2+}$, which not only convert to Co and Co_3O_4, but also form a big amount of CoN after calcination.

Raman spectra in Fig. 2(b) demonstrate that all samples have two characteristic bumps near 1591 and 1366 cm^{-1}, relating to G band (graphitized ordered carbon) and D band (disordered carbon). In general, the graphitization degree of carbonaceous materials can be characterized by the strength ratio of D and G band (I_D/I_G) [33]. The I_D/I_G values of GO, NG, $Co/Co_3O_4/G$, and $Co/Co_3O_4/CoN/NG$ are 0.93, 1.15, 1.12, and 1.23, respectively. It is reasonable that the value for GO is significantly lower than those of other samples, indicating higher graphitization degree, because the carbon lattices are not interrupted by nanoparticles and heteroatoms for pure graphene. After immersing with Co^{2+} or/and ammonia followed by calcination, the as-formed cobalt-based compound particles and the N atoms are partially inserted into graphene lattice, which lower their orderness and lead to increased I_D/I_G ratios for NG, $Co/Co_3O_4/G$, and $Co/Co_3O_4/CoN/NG$ samples.

The surface elemental states of $Co/Co_3O_4/CoN/NG$ are further analyzed by XPS. Fig. 3(a) shows the fitting result of Co $2p_{3/2}$, in which 786.6 eV is the satellite peak and the signal peaks at 782.4, 780.9, and 779.8 eV correspond to Co–N, Co–O, and Co^0, which come from CoN, Co_3O_4, and Co phases, respectively [34]. Fig. 3(b) exhibits four characteristic peaks of high-resolution N 1s spectrum at 398.5, 399.7, 400.9, and 401.6 eV, which correspond to pyridinic N, Co–N, pyrrolic N, and graphitic N, respectively. Aside from active Co–N in CoN crystalline, pyridinic N, pyrrolic N, and graphitic N come from the doped nitrogen atoms in carbon matrix, which improve the ORR catalytic activity by optimizing the electronic structure of nearby carbon lattice [35]. As for the O 1s high resolution spectrum in Fig. 3(c), there are

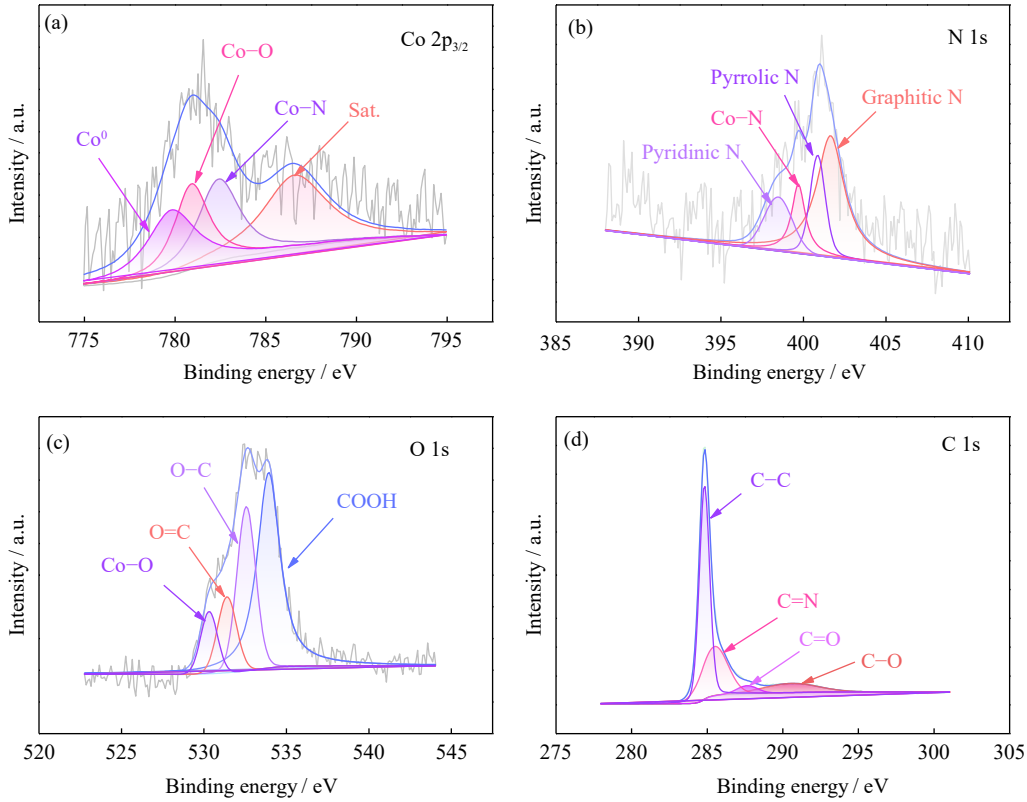

Fig. 3. XPS spectra of $Co/Co_3O_4/CoN/NG$: (a) Co $2p_{3/2}$; (b) N 1s; (c) O 1s; (d) C 1s.

four peaks at 530.3, 531.4, 532.5, and 533.9 eV, corresponding to Co–O, O=C, O–C, and COOH bonds, respectively [36]. Co–O reflects the signal of Co_3O_4, while the rest come from the doping or surface O on carbon matrix. The fitting result of C 1s spectrum shows four types of carbon bonding as shown in Fig. 3(d), belonging to C–C (284.6 eV), C–O (286.8 eV), C=O (290.5 eV), and C–N (285.3 eV) [37]. For pristine GO, the deconvoluted C 1s spectrum only comprises C–C, C–O, and C=O signals, due to the absence of doping N (Fig. S2).

3.2. Electrocatalytic performance

Cyclic voltammetry was used for preliminary judgment of the catalytic activity for Co/Co_3O_4/CoN/NG. As can be seen from Fig. 4(a), there are no reduction peaks in the CV curve tested in nitrogen saturated electrolyte; however, a reduction peak appears in that tested in oxygen saturated electrolyte, indicating that the catalyst has prominent electrocatalytic activity for ORR. To further study the electrocatalytic behavior, LSV curves of Co/Co_3O_4/CoN/NG and other control samples were tested (Fig. 4(b)). The results show that the limiting current density of Co/Co_3O_4/CoN/NG is 4.60 mA·cm^{-2}, almost reaching the value of most advanced commercial Pt/C (5.12 mA·cm^{-2}), and extremely better than that of the comparison samples. The onset potentials of GO, NG, and Co/Co_3O_4/NG only reach 0.85, 0.85, and 0.86 V vs. RHE, respectively, and all of them are lower than the value of Co/Co_3O_4/CoN/NG (0.89 V vs. RHE). In addition, the half-wave potential of Co/Co_3O_4/CoN/NG (0.80 V vs. RHE) is similar with Pt/C (0.81 V vs. RHE). The excellent electrocatalytic performance of Co/Co_3O_4/CoN/NG is derived from its multicomponent system and two-dimensional structure. Multiple components of Co, Co_3O_4, and CoN co-exist in the nanoparticles, which synergistically contribute to the high electrocatalytic activity for ORR. On the other hand, N doped graphene as matrix has a two-dimensional nanosheet structure, which provides many additional active sites and rapid mass/electron transport routes for ORR. Fig. 4(c) displays the Tafel curves for all samples. It is obvious that Co/Co_3O_4/CoN/NG has the smallest Tafel slope (48 mV·dec^{-1}) by comparison of those of GO, NG, Co/Co_3O_4/G, and Pt/C (74, 66, 59, and 97 mV·dec^{-1}), indicating faster ORR kinetics of Co/Co_3O_4/CoN/NG than other samples. In addition, Fig. 4(d) displays the Nyquist plots of different samples and the inset presents the scheme of equivalent circuit. The corresponding simulated impedance results are shown in Table 1. Reasonably, the resistance of electrolyte solution (R_s) and intrinsic resistance of catalyst (R_c) do not deviate much for all samples. However, the charge transfer resistance (R_t), which reflects the ORR efficiency on electrocatalyst, varies greatly. No doubt, Co/Co_3O_4/CoN/NG exhibits the smallest value (R_t = 296 Ω), which coincides well with its higher catalytic activity than the other samples. The parameter of CPE refers to the constant phase element for nonideal capacitance fitting.

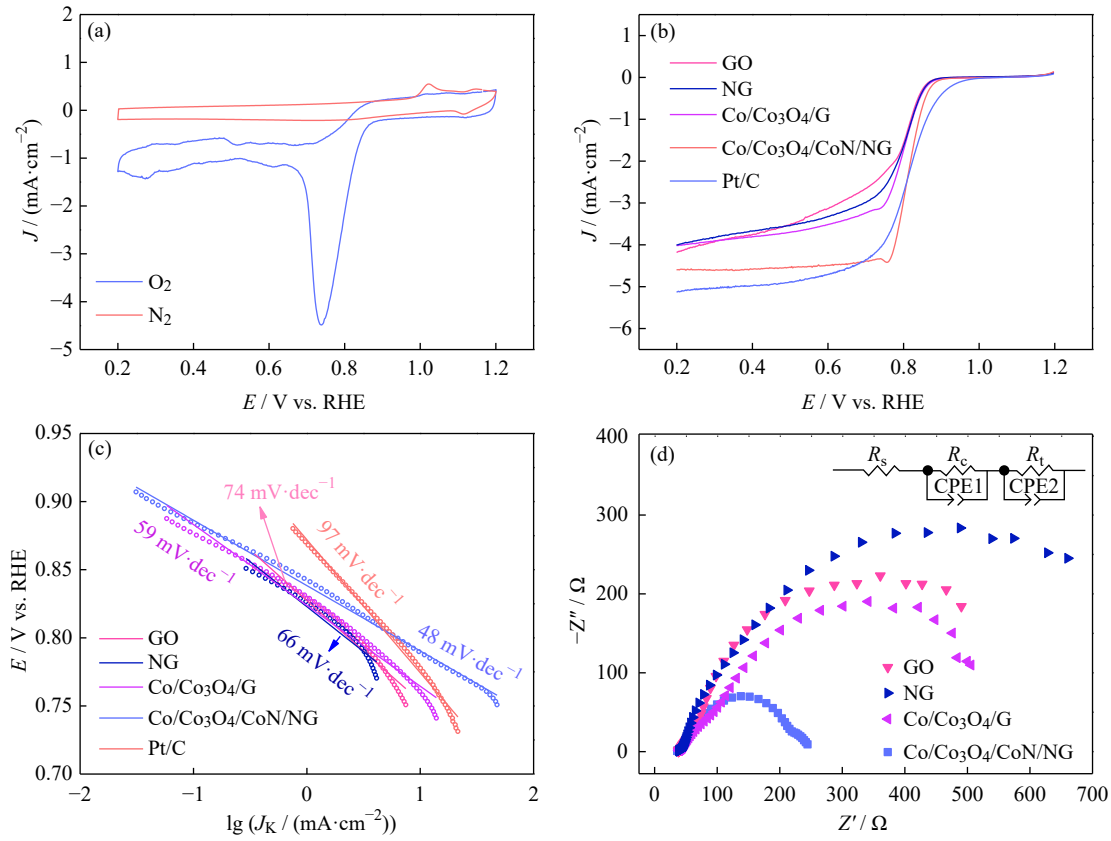

Fig. 4. (a) CV curves of Co/Co_3O_4/CoN/NG at 50 mV·s^{-1} (*J*—Current density, *E*—Potential); (b) LSV results at 5 mV·s^{-1} with 1600 r/min; (c) Tafel plots of different catalysts; (d) Nyquist plots at an electrocatalytic potential of 0.85 V vs. RHE with the inset showing the diagram of equivalent circuit.

Table 1. Simulated parameters of equivalent circuit from EIS results

Samples	R_s / Ω	R_c / Ω	R_t / Ω	CPE1	CPE2
GO	72.56	21.73	1340	0.001	0.009
NG	76.81	25.64	1510	0.003	0.012
$Co/Co_3O_4/G$	71.71	26.49	375	0.002	0.008
$Co/Co_3O_4/CoN/NG$	61.31	21.4	296	0.001	0.009

To further investigate the ORR kinetics on $Co/Co_3O_4/CoN/NG$, LSV curves were recorded from 400 to 2025 r/min. Fig. 5(a) reveals that the limiting current increases with the RDE rotate at faster speeds. The presence of reduction peaks at low rotation rates is mainly due to the insufficient diffusion of oxygen to active sites [38–39]. Moreover, Fig. 5(b) displays the K-L plots fitted according to the LSV profiles. At different potentials (0.3–0.6 V vs. RHE), the plots almost coincide. This indicates that the ORR process exhibits first-order kinetics relative to the dissolved O_2 concentration. In addition, the electron transfer numbers (n) calculated are all about 4, verifying that $Co/Co_3O_4/CoN/NG$ transforms O_2 directly into OH^- with a four-electron pathway. As durability is an important factor to evaluate catalyst performance, the current retention rates of $Co/Co_3O_4/CoN/NG$ and Pt/C were evaluated with and without the addition of methanol by chronoamperometry at a constant potential of 0.6 V vs. RHE. According to Fig. 5(c), the current density of $Co/Co_3O_4/CoN/NG$ retains 85.0% of the original value after 20000 s, while the retention of Pt/C is only 57.5%, which proves that $Co/Co_3O_4/CoN/NG$ is more stable than commercial Pt/C. In order to study the tolerance of the catalyst to methanol, the electrolyte was injected with methanol in the process of chronoamperometry to study the current retention curves. As can be seen from Fig. 5(d), methanol causes slight current fluctuation for $Co/Co_3O_4/CoN/NG$, and the retention rate is 84.5% after 2000 s. In contrast, injection of methanol had a great impact on Pt/C, causing sharp current decrease, indicating that $Co/Co_3O_4/CoN/NG$ has better tolerance to methanol than Pt/C.

According to the forementioned results and discussion, the excellent catalytic performance of $Co/Co_3O_4/CoN/NG$ for ORR can be explained from the following two points: (1) cobalt-based multicomponent nanoparticles, in which Co_3O_4, CoN, and Co cooperate to realize high catalytic activity and relatively good conductivity; (2) N-doped graphene with two-dimensional nanosheet structure as matrix, which provides large accessible surface area carrying sufficient active sites, and efficient routes for mass/electron transport.

3.3. Zinc–air battery performance

To explore the application prospect of $Co/Co_3O_4/CoN/NG$, ZAB was constructed with $Co/Co_3O_4/CoN/NG$ or Pt/C as cathode catalyst. Fig. 6(a) displays the polarization curves, together with their power density plots of ZABs based with $Co/Co_3O_4/CoN/NG$ and Pt/C as cathodic catalysts. The max-

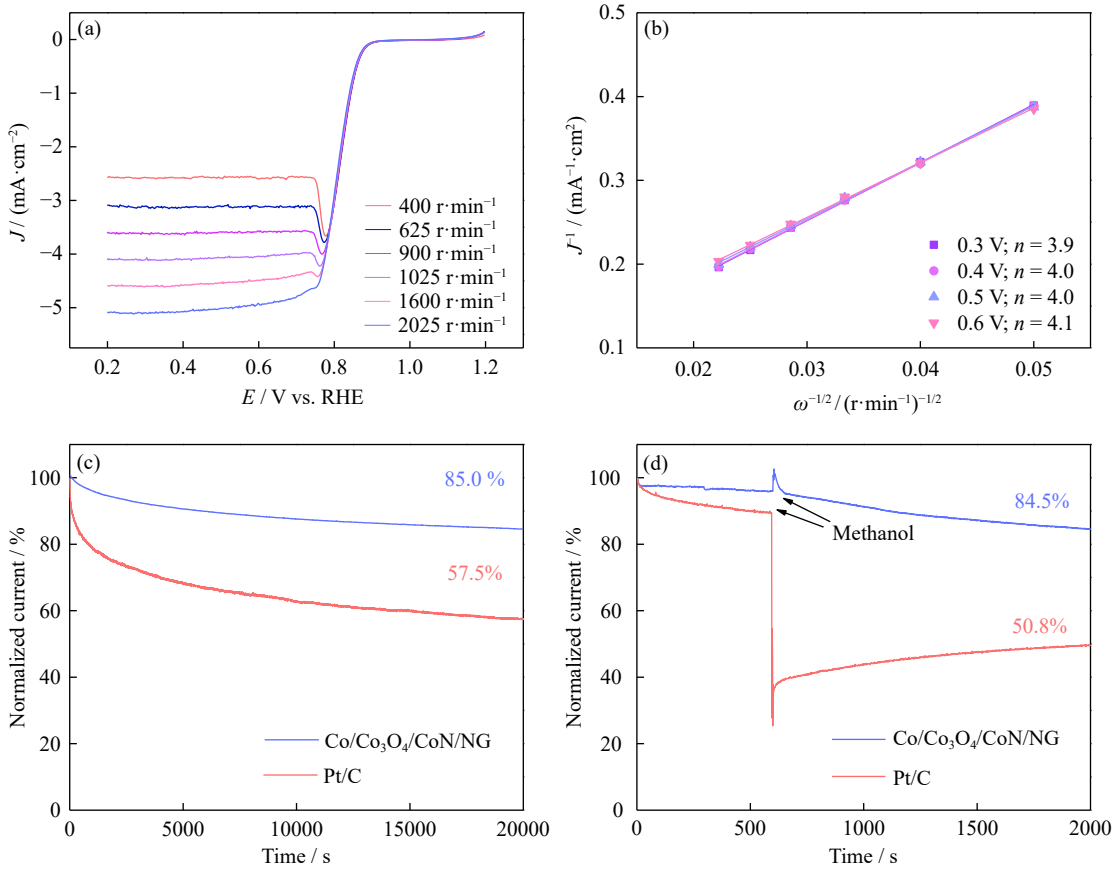

Fig. 5. (a) LSV curves for $Co/Co_3O_4/CoN/NG$ with RDE rotating at different speeds; (b) Koutecky–Levich plots for $Co/Co_3O_4/CoN/NG$ at different potentials; (c, d) durability and methanol tolerance of $Co/Co_3O_4/CoN/NG$ and Pt/C at 1600 r/min.

imum power density of $Co/Co_3O_4/CoN/NG$ battery is 120.7 $mW·cm^{-2}$, lightly lower than Pt/C (153.3 $mW·cm^{-2}$). Fig. 6(b) provides the open circuit voltage of $Co/Co_3O_4/CoN/NG$ based battery, which exhibits a high value of 1.41 V and remains stable after 20 h. As shown in Fig. 6(c), the ZAB based on $Co/Co_3O_4/CoN/NG$ still outputs a relatively high voltage of 1.22 V with almost no decay over 20 h with the discharge current density of 10 $mA·cm^{-2}$. Fig. 6(d) shows that the $Co/Co_3O_4/CoN/NG$ based battery at 10 $mA·cm^{-2}$ has the specific capacity of 843.0 $mAh·g^{-1}$, almost comparable with the Pt/C based battery (857.0 $mAh·g^{-1}$) tested under the same condition. The discharge curves at different current densities for $Co/Co_3O_4/CoN/NG$ based ZAB are shown in Fig. 6(e). Voltage platforms at 1.32, 1.29, 1.22, and 1.04 V are delivered at 5, 10, 20, and 50 $mA·cm^{-2}$, respectively, which are similar to the values of Pt/C based batteries and show excellent rate performance. Fig. 6(f) displays a photograph of two series-connected $Co/Co_3O_4/CoN/NG$ based ZABs, which light up a 2.2 V light-emitting diode. Moreover, to investigate the application prospect in secondary ZABs, $Co/Co_3O_4/CoN/NG$ was also mixed with RuO_2 before being applied as cathode catalyst. The cycling stability of $Co/Co_3O_4/$

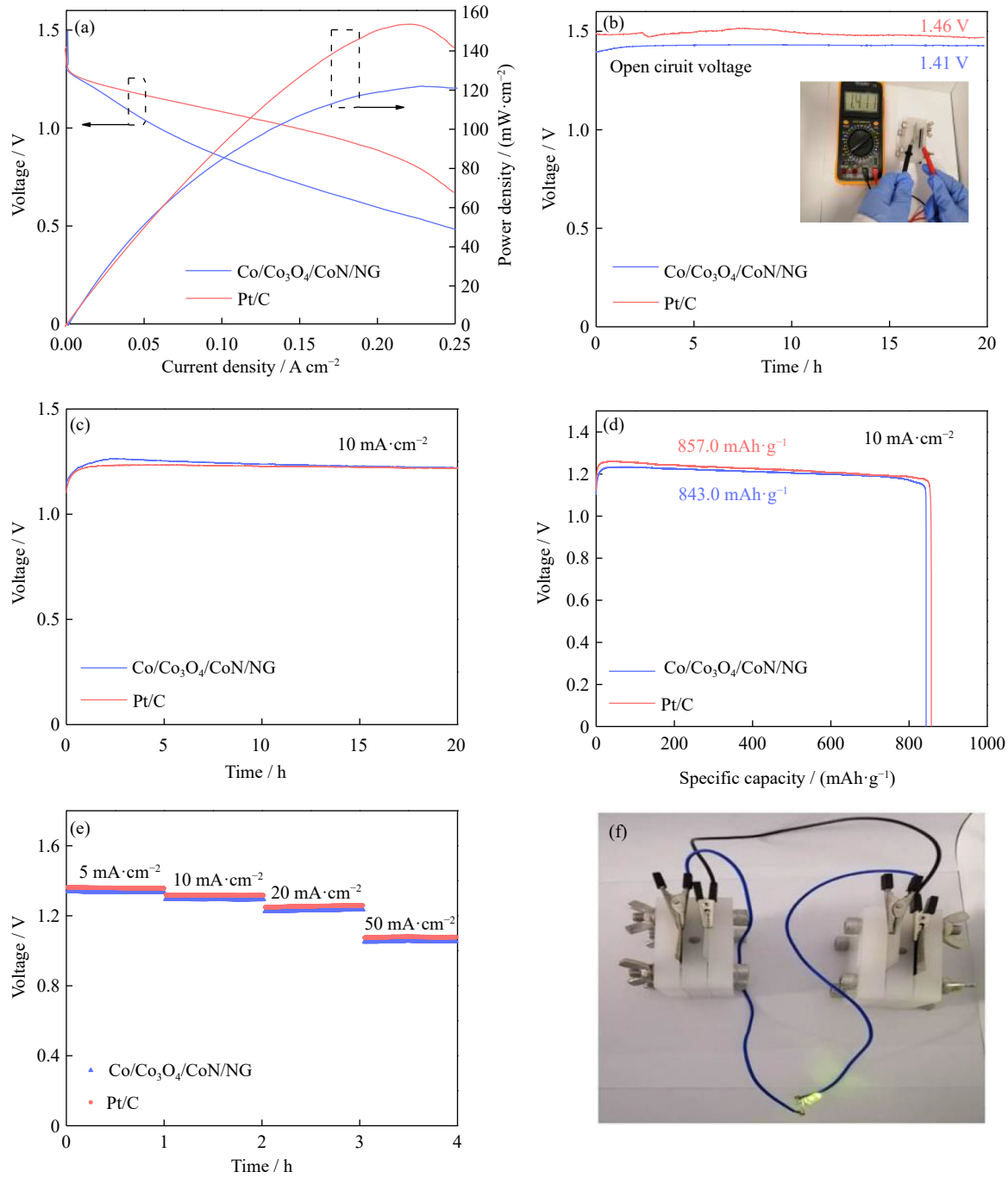

Fig. 6. (a) Polarization/power density and (b) open circuit voltage plots of ZABs with $Co/Co_3O_4/CoN/NG$ and Pt/C as cathode catalysts, and inset of (b) shows the photograph of $Co/Co_3O_4/CoN/NG$ based battery with an open circuit voltage of 1.41 V; (c) discharging voltages and (d) specific capacities at 10 $mA·cm^{-2}$; (e) discharging profiles at different current densities; (f) two series-connected $Co/Co_3O_4/CoN/NG$ based batteries to light the light-emitting diode.

CoN/NG + RuO_2-based rechargeable ZABs was studied by galvanostatic charge and discharge test at the current density of 10 mA·cm^{-2} with each cycle taking 20 min (Fig. S3). After continuous discharging and charging for more than 110 h and 220 cycles, the voltage difference of the Co/Co_3O_4/CoN/NG + RuO_2-based rechargeable battery has changed little, indicating good cycling stability. Compared with recently reported cobalt compound catalysts, the prepared Co/Co_3O_4/CoN/NG in this work shows relatively good ORR electrocatalytic property and ZAB performance in the field of open circuit voltage, half-wave potential, specific capacity, and peak power density [39−43].

4. Conclusion

In summary, cobalt-based multicomponent nanoparticles supported on nitrogen-doped graphene nanosheets (Co/Co_3O_4/CoN/NG) were prepared by a facile adsorption–complexation–calcination method. The highly dispersed Co/Co_3O_4/CoN nanoparticles and N heteroatoms provided a large number of catalytic active sites, while the graphene matrix ensured efficient charge/mass transport, leading to improved ORR electrocatalytic behaviors. The measured values for half-wave potential was 0.80 V vs. RHE and the limiting current density was 4.60 mA·cm^{-2}. Co/Co_3O_4/CoN/NG had better cycle lives and tolerance to methanol than Pt/C. Acting as cathodic catalyst for ZABs, a big open circuit voltage of 1.41 V was achieved for the battery with a high peak power density of 120.7 mW·cm^{-2} and specific capacity of 843.0 mAh·g^{-1}, which were only almost similar to those of Pt/C based counterpart. What's more, good stability and rate capability were also demonstrated for the Co/Co_3O_4/CoN/NG based battery. This study provides a simple method to prepare advanced electrocatalysts with multiple catalytic active components and efficient nanosheet structures, which is of high value in electrochemical energy conversion and storage fields.

Acknowledgements

This work was financially supported by the National Natural Science Foundation of China (No. 52102100), the Industry-University-Research Cooperation Project of Jiangsu Province, China (No. BY2021525), and the Postgraduate Research & Practice Innovation Program of Jiangsu Province, China (No. SJCX22_1944).

Conflict of Interest

The authors declare no conflict of interest.

Supplementary Information

The online version contains supplementary material available at https://doi.org/10.1007/s12613-022-2498-0.

References

[1] M. Huang, B.J. Xi, N.X. Shi, *et al*., Quantum-matter Bi/TiO_2 heterostructure embedded in N-doped porous carbon nanosheets for enhanced sodium storage, *Small Struct.*, 2(2021), No. 4, art. No. 2000085.

[2] Z.J. Liu, F.F. Zheng, W.W. Xiong, X.G. Li, A.H. Yuan, and H. Pang, Strategies to improve electrochemical performances of pristine metal-organic frameworks-based electrodes for lithium/sodium-ion batteries, *SmartMat*, 2(2021), No. 4, p. 488.

[3] D.W. Wang and D.S. Su, Heterogeneous nanocarbon materials for oxygen reduction reaction, *Energy Environ. Sci.*, 7(2014), No. 2, p. 576.

[4] X.J. Zheng, X.C. Cao, K. Zeng, *et al*., A self-jet vapor-phase growth of 3D FeNi@NCNT clusters as efficient oxygen electrocatalysts for zinc–air batteries, *Small*, 17(2021), No. 4, art. No. e2006183.

[5] P.Q. Chen, Y.X. Tai, H. Wu, Y.F. Gao, J.Y. Chen, and J.G. Cheng, Novel confinement combustion method of nanosized WC/C for efficient electrocatalytic oxygen reduction, *Int. J. Miner. Metall. Mater.*, 29(2022), No. 8, p. 1627.

[6] J. Shi, X.M. Guo, S.J. Liu, *et al*., An altered nanoemulsion assembly strategy for *in-situ* synthesis of Co2P/NP-C nanospheres as advanced oxygen reduction electrocatalyst for zinc–air batteries, *Composites Part B*, 231(2022), p. 109589.

[7] X.M. Guo, C. Qian, R.H. Shi, *et al*., Biomorphic Co–N–C/CoO_x composite derived from natural chloroplasts as efficient electrocatalyst for oxygen reduction reaction, *Small*, 15(2019), p. 1804855.

[8] J. Wang, X.P. Cheng, Z.L. Li, *et al*., Perovskite $Sr_{0.9}Y_{0.1}CoO_{3-\delta}$ nanorods modified with CoO nanoparticles as a bifunctional catalyst for rechargeable Li−O_2 batteries, *ACS Appl. Energy Mater.*, 1(2018), No. 10, p. 5557.

[9] J.J. Bian, X.P. Cheng, X.Y. Meng, *et al*., Nitrogen-doped $NiCo_2O_4$ microsphere as an efficient catalyst for flexible rechargeable zinc–air batteries and self-charging power system, *ACS Appl. Energy Mater.*, 2(2019), No. 3, p. 2296.

[10] Y. Wang, J. Li, and Z.D. Wei, Transition-metal-oxide-based catalysts for the oxygen reduction reaction, *J. Mater. Chem. A*, 6(2018), No. 18, p. 8194.

[11] C. Qian, X.M. Guo, W. Zhang, *et al*., Co_3O_4 nanoparticles on porous bio-carbon substrate as catalyst for oxygen reduction reaction, *Microporous Mesoporous Mater.*, 277(2019), p. 45.

[12] Y.N. Hou, Z. Zhao, H. Zhang, *et al*., Designed synthesis of cobalt nanoparticles embedded carbon nanocages as bifunctional electrocatalysts for oxygen evolution and reduction, *Carbon*, 144(2019), p. 492.

[13] I. A, L. Xiaobo, Z.H. pu, *et al*., From 3D ZIF nanocrystals to Co–N_x/C nanorod array electrocatalysts for ORR, OER and Zn–air batteries, *Adv. Funct. Mater.*, 28(2018), No. 5, art. No. 1704638.

[14] H.B. Tang, X.L. Tian, J.M. Luo, *et al*., A Co-doped porous niobium nitride nanogrid as an effective oxygen reduction catalyst, *J. Mater. Chem. A*, 5(2017), No. 27, p. 14278.

[15] P. Wei, X.G. Li, Z.M. He, *et al*., Porous N, B Co-doped carbon nanotubes as efficient metal-free electrocatalysts for ORR and Zn–air batteries, *Chem. Eng. J.*, 422(2021), art. No. 130134.

[16] X.M. Guo, W. Zhang, J. Shi, *et al*., A channel-confined strategy for synthesizing CoN–CoO_x/C as efficient oxygen reduction electrocatalyst for advanced zinc–air batteries, *Nano Res.*, 15(2022), No. 3, p. 2092.

[17] X.H. Wan, X.M. Guo, M.T. Duan, *et al*., Ultrafine CoO nanoparticles and Co–N–C lamellae supported on mesoporous carbon for efficient electrocatalysis of oxygen reduction in zinc–air batteries, *Electrochim. Acta*, 394(2021), art. No. 139135.

[18] Z.K. Yang, C.M. Zhao, Y.T. Qu, *et al*., Trifunctional self-sup-

porting cobalt-embedded carbon nanotube films for ORR, OER, and HER triggered by solid diffusion from bulk metal, *Adv. Mater.*, 31(2019), No. 12, art. No. e1808043.

[19] T.T. Gao, C.X. Zhou, Y.J. Zhang, Z.Y. Jin, H.Y. Yuan, and D. Xiao, Ultra-fast pyrolysis of ferrocene to form Fe/C heterostructures as robust oxygen evolution electrocatalysts, *J. Mater. Chem. A*, 6(2018), No. 43, p. 21577.

[20] E.Y. Choi, D.E. Kim, S.Y. Lee, and C.K. Kim, Electrocatalytic activity of nitrogen-doped holey carbon nanotubes in oxygen reduction and evolution reactions and their application in rechargeable zinc–air batteries, *Carbon*, 166(2020), p. 245.

[21] W.M. Zhang, X.Y. Yao, S.N. Zhou, *et al*., ZIF-8/ZIF-67-derived Co-N_x-embedded 1D porous carbon nanofibers with graphitic carbon-encased Co nanoparticles as an efficient bifunctional electrocatalyst, *Small*, 14(2018), No. 24, p. 1800423.

[22] X. Wang, X.Y. Li, C.B. Ouyang, *et al*, Nonporous MOF-derived dopant-free mesoporous carbon as an efficient metal-free electrocatalyst for the oxygen reduction reaction, *J. Mater. Chem. A*, 4(2016), No. 24, p. 9370.

[23] J. Lim, J.W. Jung, N.Y. Kim, *et al*., N_2-dopant of graphene with electrochemically switchable bifunctional ORR/OER catalysis for Zn–air battery, *Energy Storage Mater.*, 32(2020), p. 517.

[24] C.Z. Zhu and S.J. Dong, Recent progress in graphene-based nanomaterials as advanced electrocatalysts towards oxygen reduction reaction, *Nanoscale*, 5(2013), No. 5, p. 1753.

[25] X.W. Wang, G.Z. Sun, P. Routh, D.H. Kim, W. Huang, and P. Chen, Heteroatom-doped graphene materials: Syntheses, properties and applications, *Chem. Soc. Rev.*, 43(2014), No. 20, p. 7067.

[26] W.H. Chen, G.C. Zhang, D. Li, S.G. Ma, B.D. Wang, and X. Jiang, Preparation of nitrogen-doped porous carbon from waste polyurethane foam by hydrothermal carbonization for H_2S adsorption, *Ind. Eng. Chem. Res.*, 59(2020), No. 16, p. 7447.

[27] J.Q. Sun, S.E. Lowe, L.J. Zhang, *et al*., Ultrathin nitrogen-doped holey carbon@graphene bifunctional electrocatalyst for oxygen reduction and evolution reactions in alkaline and acidic media, *Angew. Chem. Int. Ed.*, 130(2018), No. 50, p. 16749.

[28] J. Oh, S. Park, D. Jang, Y. Shin, D. Lim, and S. Park, Metal-free N-doped carbon blacks as excellent electrocatalysts for oxygen reduction reactions, *Carbon*, 145(2019), p. 481.

[29] J.P. Wang, G.K. Han, L.G. Wang, *et al*., ZIF-8 with ferrocene encapsulated: A promising precursor to single-atom Fe embedded nitrogen-doped carbon as highly efficient catalyst for oxygen electroreduction, *Small*, 14(2018), No. 15, art. No. 1704282.

[30] D. Wang, X.N. Pan, P.X. Yang, *et al*., Transition metal and nitrogen co-doped carbon-based electrocatalysts for the oxygen reduction reaction: From active site insights to the rational design of precursors and structures, *ChemSusChem*, 14(2021), No. 1, p. 33.

[31] M.R. Wu, M.Y. Gao, S.Y. Zhang, *et al*., High-performance lithium-sulfur battery based on porous N-rich g-C_3N_4 nanotubes *via* a self-template method, *Int. J. Miner. Metall. Mater.*, 28(2021), No. 10, p. 1656.

[32] M.T. Duan, M.R. Wu, K. Xue, *et al*., Preparation of Co/SnO_2@NC/S composites as high-stability cathode material for lithium-sulfur batteries, *Int. J. Miner. Metall. Mater.*, 28(2021), No. 10, p. 1647.

[33] J.L. Chen, X.M. Guo, M.Y. Gao, *et al*., Free-supporting dual-confined porous Si@c-ZIF@carbon nanofibersfor high-performance lithium-ion batteries, *Chem. Commun.*, 57(2021), p. 10580.

[34] C. Cai, M.Y. Wang, S.B. Han, *et al*., Ultrahigh oxygen evolution reaction activity achieved using Ir single atoms on amorphous CoO_x nanosheets, *ACS Catal.*, 11(2021), No. 1, p. 123.

[35] J.Y. Qin, Z.W. Liu, D.Y. Wu, and J. Yang, Optimizing the electronic structure of cobalt via synergized oxygen vacancy and Co–N–C to boost reversible oxygen electrocatalysis for rechargeable Zn–air batteries, *Appl. Catal. B*, 278(2020), art. No. 119300.

[36] J.T. Jin, X.G. Fu, Q. Liu, and J.Y. Zhang, A highly active and stable electrocatalyst for the oxygen reduction reaction based on a graphene-supported g-C_3N_4@cobalt oxide core-shell hybrid in alkaline solution, *J. Mater. Chem. A*, 1(2013), No. 35, p. 10538.

[37] D.W. Chen, C.L. Dong, Y.Q. Zou, *et al., In situ* evolution of highly dispersed amorphous CoO_x clusters for oxygen evolution reaction, *Nanoscale*, 9(2017), No. 33, p. 11969.

[38] W.Q. Kong, K.K. Yao, X.D. Duan, Z.G. Liu, and J.W. Hu, Holey Co, N-codoped graphene aerogel with in-plane pores and multiple active sites for efficient oxygen reduction, *Electrochim. Acta.*, 269(2018), p. 544.

[39] S.W. Liu, H.M. Zhang, Q. Zhao, *et al*., Metal-organic framework derived nitrogen-doped porous carbon@graphene sandwich-like structured composites as bifunctional electrocatalysts for oxygen reduction and evolution reactions, *Carbon*, 106(2016), p. 74.

[40] T.T. Li, Y.X. Lu, S.S. Zhao, Z.D. Gao, and Y.Y. Song, Co_3O_4-doped Co/CoFe nanoparticles encapsulated in carbon shells as bifunctional electrocatalysts for rechargeable Zn–air batteries, *J. Mater. Chem. A*, 6(2018), No. 8, p. 3730.

[41] S. Mao, Z.H. Wen, T.Z. Huang, Y. Hou, and J.H. Chen, High-performance bi-functional electrocatalysts of 3D crumpled graphene–cobalt oxide nanohybrids for oxygen reduction and evolution reactions, *Energy Environ. Sci.*, 7(2014), No. 2, p. 609.

[42] Z.Y. Guo, F.M. Wang, Y. Xia, *et al., In situ* encapsulation of core-shell-structured Co@Co_3O_4 into nitrogen-doped carbon polyhedra as a bifunctional catalyst for rechargeable Zn–air batteries, *J. Mater. Chem. A*, 6(2018), No. 4, p. 1443.

[43] P. Yu, L. Wang, F.F. Sun, *et al*., Co nanoislands rooted on Co–N–C nanosheets as efficient oxygen electrocatalyst for Zn–air batteries, *Adv. Mater.*, 31(2019), No. 30, art. No. 1901666.